JACS
JOURNAL OF THE AMERICAN CHEMICAL SOCIETY
pubs.acs.org/JACS
Article

Magnetoelectric Coupling in a Mn_4Na–Organic Complex under Pulsed Magnetic Fields up to 73 T

James Paris Wampler,* Shuanglong Liu, Dibya Jyoti Mondal, Magdalena Owczarek, Shengzhi Zhang, Ping Wang, Miguel Gakiya-Teruya, Minseong Lee, Hai-Ping Cheng, Michael Shatruk,* and Vivien S. Zapf*

Cite This: *J. Am. Chem. Soc.* 2024, 146, 32383–32391
Read Online
ACCESS | Metrics & More | Article Recommendations | Supporting Information

ABSTRACT: Research on the magnetoelectric (ME) effect (or spin-electric coupling) in molecule-based magnetic materials is a relatively nascent but promising topic. Molecule-based magnetic materials have diverse magnetic functionalities that can be coupled to electrical properties. Here we investigate a realization of ME coupling that is fundamental but not heavily studied—the coupling of magnetic spin level crossings to changes in electric polarization. A mixed-valence Mn_4Na complex with a total ground-state spin S = 5/2 under zero magnetic field and S = 17/2 under high magnetic field undergoes a cascade of ground-state level crossings of the S_z states with increasing magnetic field. Magnetization and electrical polarization measurements under pulsed magnetic fields up to 73 T show that each spin level crossing is accompanied by a significant change in electric polarization that is an even function of the applied magnetic field. A molecular Hamiltonian describing antiferromagnetic exchange in a distorted tetrahedron of three Mn^{III} and one Mn^{II} ions matches the data well. We conclude that the ME coupling is caused by magnetostriction within the polar molecule as it distorts to lower its magnetic exchange energy.

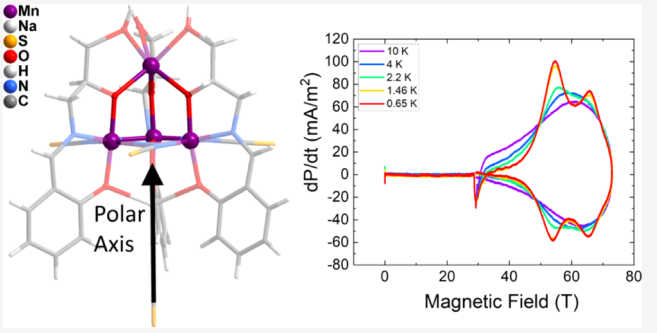

INTRODUCTION

The magnetoelectric (ME) effect describes coupling between an applied magnetic field acting on a material and the material's electrical polarization or the coupling between an applied electric field and the material's magnetization.[1−5] Under static conditions, the effect was first experimentally demonstrated by Astrov and Rado and Folen ca. 1960.[6,7] Since then, the ME effect has been considered promising for various technological applications,[4,8] including ME magnetic field sensors[9] and ME random access memory, in which information can be encoded in both the magnetization and polarization states of a device, allowing for higher information storage density.[10,11] To actualize future applications, new materials are needed with stronger ME coupling or novel ME coupling behavior. To date, however, the majority of efforts have focused on studying inorganic materials such as multiferroic oxides and ferromagnetic/ferroelectric composites.

The recent interest in ME coupling in molecule-based magnetic materials parallels the development of molecular magnets for magnetic storage, quantum sensing, and quantum information technologies.[12−14] Implementation of molecule-based ME coupling provides a route to sense and control spins electrically,[15−17] and several works have reported such coupling in molecular magnets,[18,19] single-molecule magnets,[20−24] metal−organic frameworks,[25−28] and spin-crossover complexes.[29−32] ME coupling was also proposed in spin-frustrated molecular triangles,[15,16,33] and recently detected using electron spin resonance measurements.[20−22]

In order for a material to exhibit net electric polarization, the crystalline lattice must have a unique polar axis that hosts the electric polarization. This polarity can be either intrinsic to the underlying crystalline lattice or introduced by the magnetic spin configuration, which in turn distorts the lattice to induce electric polarization. The "lattice" here refers to both the charged ions in a static configuration and the electrons in orbitals, both of which can contribute to the net electric moment. In either case, coupling between the static magnetization and electric polarization can result because the magnetic moments will exert magnetostriction on the lattice, in an attempt to alter the magnetic interactions and thereby minimize the magnetic energy. This distortion is opposed by the strain energy of the lattice. As a result, a small net distortion of the lattice can alter a net electric polarization of a

Received: June 7, 2024
Revised: October 27, 2024
Accepted: October 29, 2024
Published: November 13, 2024

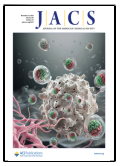

https://doi.org/10.1021/jacs.4c07759
J. Am. Chem. Soc. 2024, 146, 32383−32391

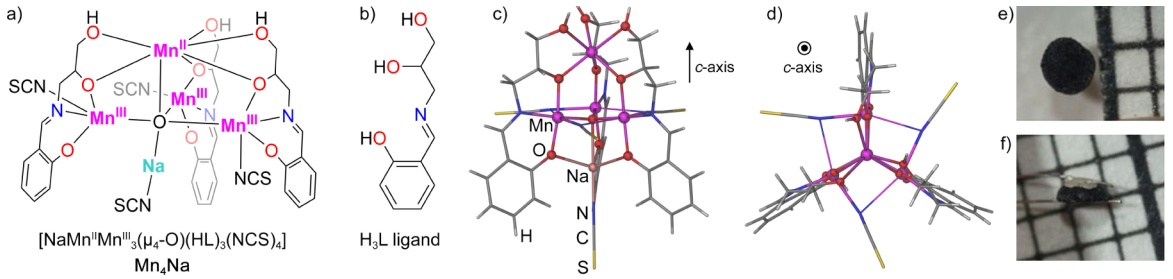

Figure 1. Structural formula of **Mn$_4$Na** (a) and the H$_3$L ligand precursor (b). The side (c) and top (d) views of the molecular structure of **Mn$_4$Na** and photos of a typical single-crystal sample viewed down (e) and perpendicular (f) to the *c* axis of the trigonal lattice. Panel (f) also shows a typical sample with leads attached to the {001} faces by means of silver paint for electrical polarization measurements.

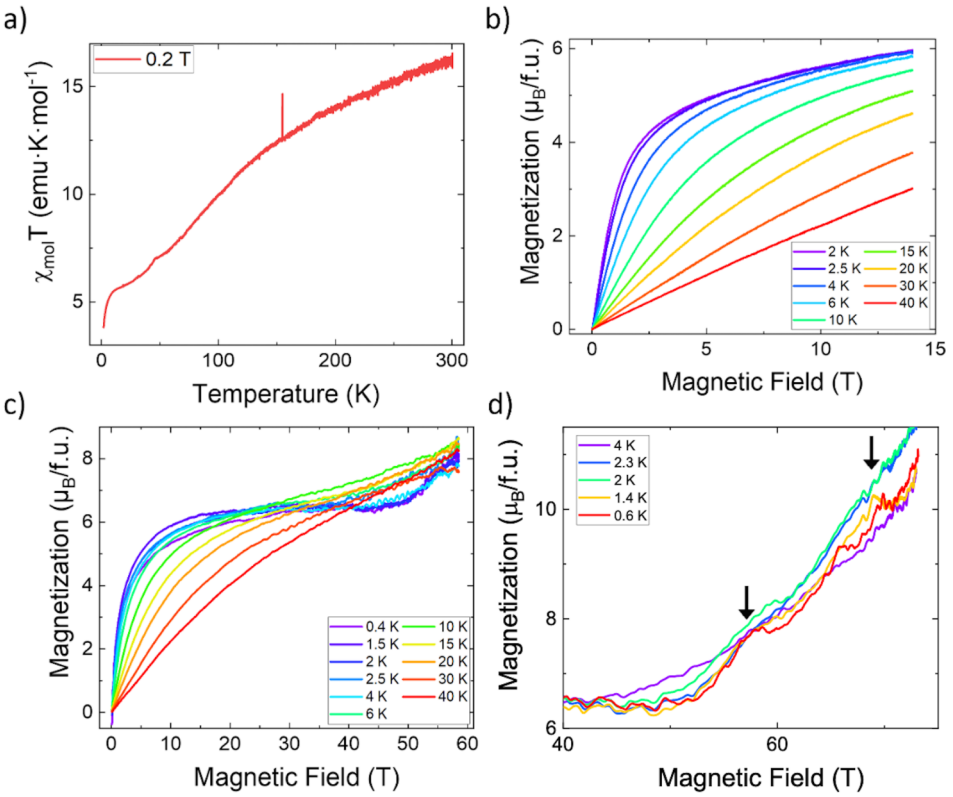

Figure 2. (a) The temperature dependence of χT measured on a single crystal of **Mn$_4$Na** in the cooling regime under applied magnetic field H = 0.2 T. (b) Magnetic field-dependent magnetization isotherms measured under DC magnetic field, with temperatures ranging from 40 K (red) to 2 K (purple). (c) Magnetic field-dependent magnetization isotherms measured under a 65 T short-pulse magnetic field with temperatures ranging from 40 K (red) to 0.4 K (purple); the magnetization axis was calibrated using the DC measurements shown in (b). (d) Magnetic field-dependent magnetization isotherms measured with the pulsed 73 T pulsed magnet. Arrows indicate onset of plateaus above 50 T.

polar lattice or break symmetry to introduce such polarization in a previously nonpolar lattice. In certain situations,[2,15,16,34] the coupling between the magnetization and the electric field can be odd (having a linear leading term) if appropriate symmetries are broken.

There are several advantages to searching for the ME effect in molecule-based magnetic materials. First, synthetic tunability of the molecular structure allows tuning a complex molecule toward desired magnetic properties. Second, molecule-based magnetic materials typically have soft structures, which can lead to very strong strain-mediated ME coupling, among other novel effects. On the other hand, such softness poses a challenge in carrying out some measurements without introducing external strain. For example, to demonstrate ME coupling through an electrical polarization measurement, it is critical to achieve good contact between electrical leads and the crystal, which unavoidably leads to some strain being applied to the soft lattice of a molecule.

In this work, we demonstrate how strong ME coupling can occur at ground-state spin level crossings in a mixed-valent complex [NaMn^{II}Mn$_3^{III}$(μ$_4$-O)(HL)$_3$(NCS)$_4$] (**Mn$_4$Na**), the crystal structure of which was reported earlier by Yang et al.[35] The molecular structure features a distorted tetrahedron of antiferromagnetically coupled three Mn^{III} and one Mn^{II} ions (Figure 1a). In the past, mixed-valent Mn tetrahedra have proved fruitful avenues of research, demonstrating various types of magnetic behaviors.[36−38] More broadly, mixed-valent Mn-based complexes have an important history as single molecule magnets (SMMs), as the so-called Mn$_{12}$ was the first SMM discovered[39,40] and was the first of a large family of mixed-valent Mn-based SMMs.[41−43] Herein, we show how an applied magnetic field acting on **Mn$_4$Na** leads to ground-state

https://doi.org/10.1021/jacs.4c07759
J. Am. Chem. Soc. 2024, 146, 32383−32391

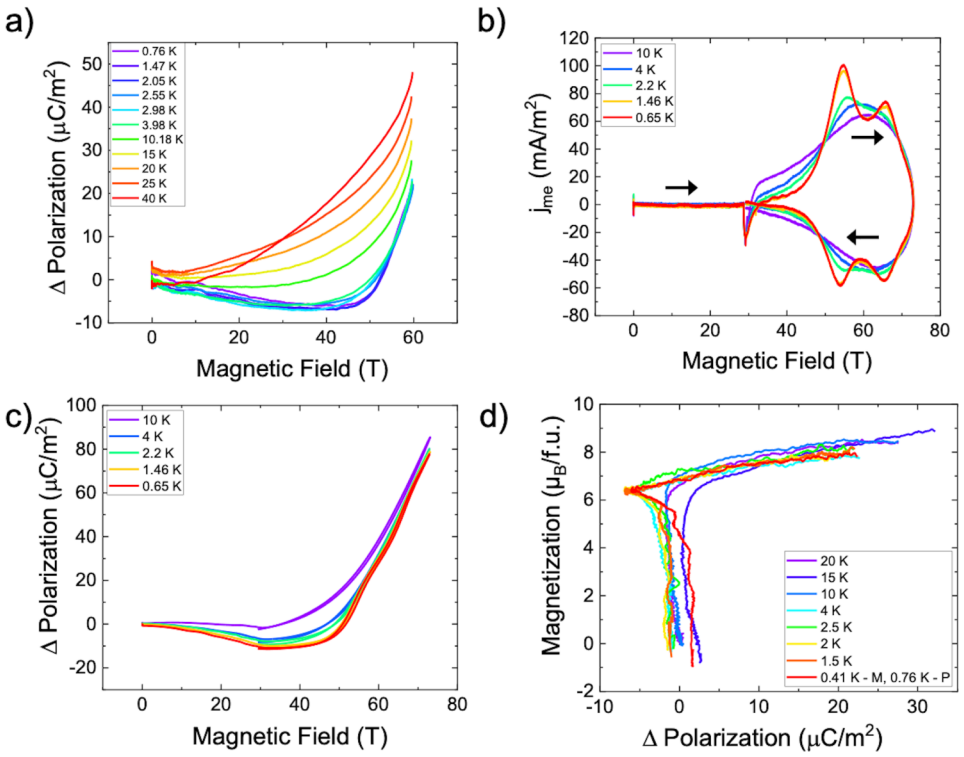

Figure 3. Electric polarization measurements with $H \perp E \parallel c$ axis: (a) change in electric polarization $\Delta P(H)$ vs magnetic field H measured in the 65 T short-pulse magnet at a nominally constant T ranging from 40 K (red) to 0.76 K (purple). (b) The ME current density (dP/dt) vs H measured in the 73 T duplex magnet with T ranging from 10 K (purple) to 0.65 K (red). Arrows indicate magnetic field sweep direction. (c) $\Delta P(H)$ obtained by integrating (b) over time. (d) Magnetization measurement from Figure 2c plotted against ΔP measurement from (a).

spin level crossings that produce jumps in the electric polarization. Theoretical treatment of this mixed-valence complex provides a satisfactory agreement with the experimental results.

RESULTS AND DISCUSSION

The neutral complex **Mn_4Na** crystallizes in the polar, trigonal space group $R3c$. It contains a mixed-valent tetrahedral $[Mn_4(\mu_4\text{-}O)(\mu_2\text{-}O_{alkoxide})_3]^{6+}$ core (Figure 1a) with peripheral ligation provided by three bridging monodentate NCS^- ligands and three bridging tetradentate HL^{2-} ligands, obtained by double deprotonation of the ligand precursor H_3L = 3-(2-hydroxybenzylideneamino)propane-1,2-diol (Figure 1b). A Na^+ ion, coordinated by the three dianionic HL^{2-} ligands and an additional terminal NCS^- ligand, completes a trigonal-bipyramidal Mn_4Na cluster, with the axis of the bipyramid aligned with the c axis of the trigonal lattice (Figure 1c). The asymmteric unit contains one-third of the complex molecule, which resides on the 3-fold symmetry axis.

The Mn^{II} ion in the apex of the bipyramid has a distorted octahedral coordination formed by six O atoms of the three HL^{2-} ligands. Each equatorial Mn^{III} ion resides in a distorted octahedral environment. Two alkoxide O atoms and one imino N atom of an HL^{2-} ligand, as well as the μ_4-O^{2-} oxide ion in the center of the bipyramid, form shorter Mn^{III}-ligand distances at 1.902 Å, 1.907 Å, 1.947 Å, and 1.907 Å, respectively. In contrast, two N-bound NCS^- ligands furnish the N−Mn−N axis of the Mn^{III} coordination octahedron with substantially elongated Mn−N bonds that define the direction of the Jahn−Teller distortion axis of each Mn^{III} ion. One of the NCS^- ligands binds to the Mn^{III} ion in a more common "head-on" fashion, with the Mn−N−C angle of 166.7° and the Mn−N bond length of 2.215 Å, while the other NCS^- ligand coordinates "sideways", with the Mn−N−C angle of 110.2° and a much longer and weaker Mn−N bond at 2.739 Å. Each NCS^- ligand thus acts as an additional bridge between two Mn^{III} ions (Figure 1d). The three Mn^{III} ions form an equilateral triangle centered by the μ_4-O^{2-} ion that is shifted by 0.262 Å from the center of the triangle toward the apical Na^+ ion.

We would like to point out that the same crystal structure was reported earlier by Yang et al.,[35] but here we provide a better quality refinement of this structure, with more reasonable bond lengths (see the Supporting Information for further details).

The Jahn−Teller axes of the three Mn^{III} ions lie approximately in the equatorial plane of the trigonal-bipyramidal metal cluster (Figure 1). An applied magnetic field acting on the antiferromagnetically coupled metal centers might cause significant magnetostriction in such molecular structure with pronounced local magnetic anisotropies. As a result, magneto-electric coupling can be achieved by the applied magnetic field affecting the bulk magnetic and electric polarization.

Macroscopically, single crystals of **Mn_4Na** were obtained as black polyhedra with the shape approximating an oblate hemispheroid (Figure 1e,f). Magnetization measurements were performed on a 0.51 mg single-crystal sample using a quantum design physical property measurement system (PPMS) equipped with a vibrating sample magnetometer (VSM) option. The magnetic field was applied perpendicular to the c axis. The product of magnetic susceptibility (χ) and temperature (T) is plotted as a function of T in Figure 2a. χT decreases with temperature until $T \sim 50$ K, before

https://doi.org/10.1021/jacs.4c07759
J. Am. Chem. Soc. 2024, 146, 32383−32391

plateauing at ∼6.5 emu·K·mol^{-1} and then sharply decreasing at lower T. This behavior indicates antiferromagnetic exchange between the Mn ions, in agreement with the earlier report.[35]

Magnetic field-dependent magnetization (M) was measured with the applied magnetic field (H) perpendicular to the c axis of the crystal, as in the temperature dependent measurements. Measurements performed under DC magnetic field (Figure 2b) revealed typical paramagnetic behavior, with $M(H)$ approaching saturation at lower values of H at lower T and higher values of H at higher T. Even at the lowest temperature of 2 K, the $M(H)$ curve did not reach saturation. This behavior will be discussed more thoroughly below.

Further, the magnetic behavior was probed under pulsed magnetic fields up to 60 T, with H perpendicular to the c axis, applied by means of the 65-T short-pulse magnet at the Pulsed Field Facility (PFF) of the National High Magnetic Field Laboratory (NHMFL). This magnet takes ∼8 ms to reach the maximum magnetic field of a given pulse and has a longer decay time of ∼50 ms. Isothermal magnetization measurements (Figure 2c) were taken with T varying from 0.4 to 40 K, with the sample in liquid or gaseous ^{3}He. Below ∼2.5 K, M increases until it saturates to a plateau of ∼6 μ_B/f.u. at 20 T. Above 45 T, the magnetization increases again until reaching a second plateau of ∼8 μ_B/f.u. at 55 T.

Theoretical calculations presented below (Figure 4) suggested that higher applied magnetic fields should lead to further magnetization plateaus due to successive spin level crossings. To verify such predictions, magnetic field-dependent magnetization measurements were performed using the pulsed 73 T duplex millisecond magnet at the PFF. In these measurements, the sample exhibited plateaus at ∼58 T visible up to 2 K and at ∼70 T visible up to 1.4 K, similar to the behavior observed in the 65 T short pulse magnets (Figure 2d) and in agreement with the theoretical prediction. Note that Figure 2d displays only the part of the measurement from 30 to 73 T. This is due to the nature of the 73 T duplex magnet, as discussed in the Supporting Information.

To demonstrate ME coupling in **Mn_4Na**, we probed a change in electrical polarization (ΔP) with respect to applied magnetic field. In order to achieve a good electrical contact, silver paint was applied to the surface of the crystal (Figure 1f). The measured quantity is the ME current (dP/dt), which can be integrated over time t to obtain $\Delta P(H)$. The signal increases linearly with dH/dt and the noise increases as the square root of measurement rate, which means that the signal-to-noise ratio improves as the square root of sweep rate. Electrical polarization measurements were taken by applying <10 ms magnetic field pulses with amplitude up to 60 T and a maximum magnetic field sweep rates over 10 kT/s at the onset of the pulse (see Figure S6), with the sample oriented such that $H \perp E \parallel c$ axis. Electric fields applied while cooling from 30 K to pole the sample did not affect the data (see Figure S5). The raw ME current measurements (dP/dt) are shown in Figure S4a. The integrated $\Delta P(H)$ data shown in Figure 3a demonstrate low values of $\Delta P(H)$ up to ∼50 T, at which point it sharply increases.

Similar results were obtained using the 73 T duplex magnet with maximum magnetic field sweep rates over 70 kT/s (see Figure S6). The ME current measurements in Figure 3b show extrema at ∼55 T and ∼67 T, the values very similar to the magnetic field at midpoints between the magnetization plateaus observed in Figure 2d. The electric polarization $\Delta P(H)$, calculated by integrating the ME current density over time (Figure 3c), shows qualitatively similar features to those observed for $M(H)$.

To demonstrate this similarity between $M(H)$ and $\Delta P(H)$, Figure 3d shows $M(H)$ extracted from Figure 2c and plotted against $\Delta P(H)$ from Figure 3a. This plot shows that the initial increase in M, up to the first $M(H)$ plateau of ∼6 μ_B at ∼15 T, does not strongly affect the electric polarization. Above ∼45 T, however, once the magnetization begins to increase again, there is an approximately linear relationship between the magnetization and electric polarization. This observation is consistent with the initial step in $M(H)$ being dominated by paramagnetic alignment of spins, which does not produce ME coupling. In contrast, the subsequent increases are dominated by spin level crossings, which do produce ME coupling. Although this data covers a large range in H and T, we observe that the plot of $\Delta P(M)$ is similar for all T. This supports the conclusion that above the broad plateau at ∼6 μ_B the changes in both M and H are driven by changes in the structure. Additionally, although the ME correlation is approximately linear, the behavior of the electric polarization does not change when the direction of the magnetic field is reversed (Figure S5). Therefore, $P(H)$ is an even function and cannot be globally linear.

In general, the coupling between magnetization and electric fields in materials falls into two categories: odd and even. In the odd case, $P(H)$ and $M(E)$ are odd functions where P or M depend on the direction (sign) of the applied fields H or E. Here the leading term of an expansion in the applied field is linear, thus it is often referred to as a 'linear magnetoelectric effect'.[1−3] On the other hand, in the even case, the leading term is squared and M or P does not depend on the direction of the applied field. Since static electric fields generally break spatial inversion while uniform magnetic fields break time inversion, it is rare for electric and magnetic properties to couple linearly in a solid. Thus, the even case is most common. There are however several scenarios in which such odd/linear coupling can occur. For example, the case of linear magnetoelectric (spin-electric) coupling in magnetic molecules consisting of antiferromagnetic triangles, tetrahedra, or odd-membered rings of magnetic ions has recently generated interest.[15,16,20,21,23] Here the conflicting magnetic interactions create spin patterns that break both spatial and time inversion symmetries.

In **Mn_4Na**, the antiferromagnetic tetrahedron of Mn spins might have hinted at an odd coupling mechanism. However, experimentally we find that $P(H)$ is an even function, where P is independent of reversing H. The even coupling case here results from the fact that the underlying crystal is already electrically polar, and so strain on the crystal due to e.g., magnetostriction can alter electric polarization. In particular, we expect the magnetoelectric coupling to be enhanced by the presence of Jahn−Teller axes on the Mn^{III} that can enhance the spin−lattice interactions.

Given that **Mn_4Na** has a polar c axis, the observation of ME coupling is consistent with a magnetostriction-driven ME effect. Applied magnetic field can strain the lattice because nearly all magnetic interactions (antiferromagnetic, single-ion anisotropy, g-factor, Jahn−Teller, etc.) depend on the lattice, and thus a strain in the lattice will alter the magnetic interactions. Any expansion or contraction of the molecule and its electronic orbitals would directly affect the polarization density and thus the measured electric polarization. Thus, as the compound passes through different spin levels of the

https://doi.org/10.1021/jacs.4c07759
J. Am. Chem. Soc. 2024, 146, 32383−32391

overall molecule, corresponding to different spin arrangements of the individual Mn spins, each one will strain the lattice in a different manner in order to attempt to minimize the magnetic energy, each level resulting in a different electric polarization.

Using a previously published model Hamiltonian and exchange-coupling constants,[35] we calculated the spin level crossings and $M(H)$, as shown in Figure 4a-d. These

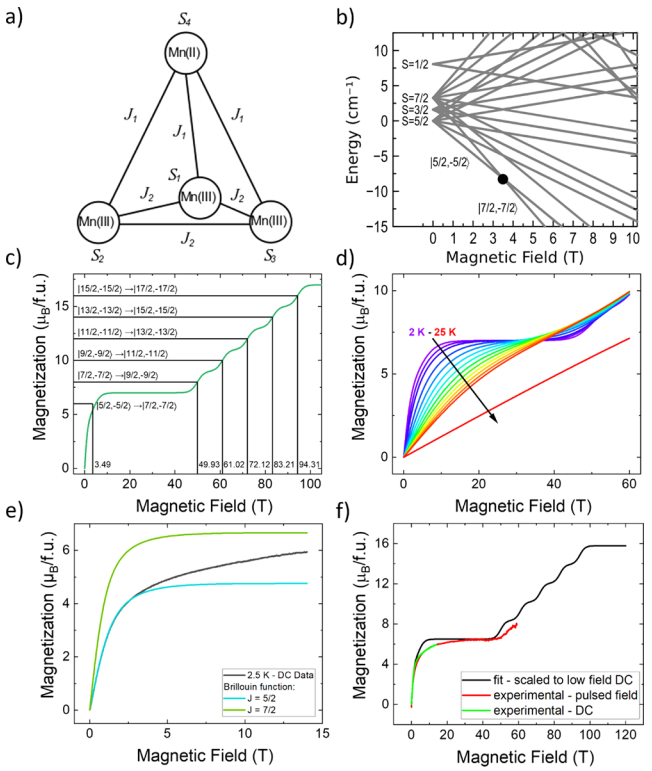

Figure 4. (a) Two different exchange coupling constants J_1 and J_2 modeled in a **Mn_4Na** molecule. J_1 is between a Mn^{III} ion and a Mn^{II} ion, and J_2 is between two Mn^{III} ions. (b) Energy levels and (c) magnetic moment at 2 K plotted against magnetic field of a **Mn_4Na** molecule. The level crossing between the $|5/2,-5/2\rangle$ and $|7/2,-7/2\rangle$ levels is marked by the dark filled circle in the panel (b). The black solid lines in the panels (c) indicate at what magnetic fields level crossings occur (values are in T) and what states are involved. (d) Magnetic moment with temperature varying from 2 K (purple) to 25 K (red). (e) Magnetization vs magnetic field $M(H)$ measurement at 2.5 K in DC magnetic fields, identical to data presented in Figure 2b, compared with Brillouin functions with $g = 2$, $T = 2$ K, $S = 5/2$, 7/2 and vertically scaled so that the $S = 5/2$ curve matches the experimental data. (f) Fitting the J_s values in the Hamiltonian in eq 1 to the same DC $M(H)$ curve at 2 K from Figure 2b.

calculations were performed after the measurements in the 65 T short-pulse magnet but before the measurements in the 73 T duplex magnet, thereby serving as explanations for the former results and successful predictions for the latter.

In the core of **Mn_4Na**, the three Mn^{III} and one Mn^{II} ions possess single-ion spin states $S = 2$ and $S = 5/2$, respectively. According to Yang et al.,[35] the molecule's magnetic susceptibility can be well described by an isotropic quantum Heisenberg model with two different exchange coupling constants, J_1 and J_2 (eq 1 and Figure 4a). In our work, the exchange coupling constants were fit to the measured DC magnetization up to 14 T at 2 K. The best-fit values of J_1 and J_2 are -5.18 cm^{-1} and -2.43 cm^{-1} respectively, which are close to the values reported by Yang et al. The g-factor was fixed at 2 for all the four spins. Possible deviations from 2 will be examined by first-principles calculations shown in the Supporting Information. Therefore, while some magnetic anisotropy could be expected for both Mn species, none was needed to reproduce the available data or accurately predict features measured later.

$$\hat{\mathcal{H}} = -2J_1 \sum_{i,j=1,4;2,4;3,4} \hat{\boldsymbol{S}}_i \cdot \hat{\boldsymbol{S}}_j - 2J_2 \sum_{i,j=1,2;1,3;2,3} \hat{\boldsymbol{S}}_i \cdot \hat{\boldsymbol{S}}_j + g \sum_{i=1}^{4} \boldsymbol{B} \cdot \hat{\boldsymbol{S}}_i \quad (1)$$

The eigenstates of the spin Hamiltonian $\hat{\mathcal{H}}$ in eq 1 are labeled by the total spin S of the four coupled Mn spins and the z axis projection m_s, since both $\hat{S}^2$ and $\hat{S}_z$ commute with $\hat{\mathcal{H}}$. The $2S + 1$ states $|S,m_s\rangle$, where $m_s \in \{-S, -S + 1, \ldots, S\}$, are degenerate under zero magnetic field (Figure 4b). The lowest energy level of the system under zero magnetic field has a total spin $S = 5/2$. The next three energy levels, which are within 10 cm^{-1}, have total spins $S = 3/2$, $S = 7/2$, and $S = 1/2$. The lowest and highest possible total spin states of the system are $S = 1/2$ and $S = 17/2$, respectively. The fact that the zero-field ground state has a value closer to the lowest total spin possible agrees with the antiferromagnetic exchange coupling in this complex. In thermal equilibrium, the occupation numbers of the states $|S,m_s\rangle$ and $|S,-m_s\rangle$ are the same due to degeneracy. As such, in this model the thermal average of magnetic moment of a **Mn_4Na** molecule is zero under zero magnetic field. When a small magnetic field is applied, the spin states are split in energy and the ground state becomes $|5/2,-5/2\rangle$. The occupation number of the $|5/2,-5/2\rangle$ state is higher than those of the higher energy states. As a result, the magnetic moment increases with the magnetic field. The slope of an energy level as a function of magnetic field is proportional to $|m_s|$. Thus, the energy of the $|7/2,-7/2\rangle$ energy level decreases faster than the energy of the $|5/2,-5/2\rangle$ level. These two energy levels cross at 3.49 T, after which the ground state is $|7/2,-7/2\rangle$ and the magnetization should saturate at 7 μ_B. Note that the discrepancy between this theoretical plateau and the experimentally observed value of ~6.2 μ_B is explained by error from the measurement of the sample mass and the diamagnetic background from the sample holder. More level crossings are expected to occur at higher magnetic fields until the spin state $|17/2,-17/2\rangle$ becomes the ground state. Figure 4c shows the magnetic field-dependent magnetization of **Mn_4Na** calculated at 2 K. The level crossings manifest as sudden jumps in magnetization at 50.0, 61.0, 72.1, 83.2, and 94.3 T. A magnetic moment plateau between two level crossings appears when the lowest energy level is (nearly) fully occupied. Such a fully occupied $|S,m_s\rangle$ ground state with $m_s = -S$ would yield a magnetic moment of $2S$ μ_B. There is not a magnetic moment plateau of 5 μ_B below 3.49 T because the energy splitting is comparable with thermal energy, and the excited states are significantly occupied. Figure 4d shows the calculated magnetic moment of a **Mn_4Na** molecule versus the measured magnetization of **Mn_4Na** at 2−25 K, demonstrating how at higher temperatures the features become washed out as more excited states are occupied even at higher magnetic fields.

It is notable that the level crossing at 3.49 T is manifested in the DC magnetization measurements, as seen in the inflection points observed in Figure 2b, but is not observable in the

https://doi.org/10.1021/jacs.4c07759
J. Am. Chem. Soc. 2024, 146, 32383−32391

pulsed magnetic field measurements. This can be confirmed by using naive calculations of the Brillouin function with $g = 2$, $S = 5/2$, 7,2 and the leading term of the curves vertically scaled so that the $S = 5/2$ curve matches the magnetization measured in DC magnetic fields and low magnetic field (Figure 4e). Using these assumptions, it is clear that while the $S = 5/2$ Brillouin function fits the data well at low magnetic field, it fails to do so above the level crossing predicted by the theory. Furthermore, the $S = 7/2$ Brillouin function saturates at nearly the same value as the magnetization measured in pulsed magnetic field saturates, ~6.2 μ_B/f.u. Figure 4f shows the theoretical model fit to the magnetization data measured in DC magnetic fields and vertically scaled so that they fit well at low magnetic field. This scaled fit does not exactly match the magnetization data, but it performs well in two respects: both show a kink at ~3.5 T where the first level crossing is predicted. Furthermore, while the theoretical model approaches the next plateau faster than the experiment, that plateau is at a similar value to the $S = 7/2$ plateau in the corresponding pulsed magnetic field magnetization measurement.

In the Supporting Information, it is shown that the discrepancy between the magnetization measured in DC and pulsed magnetic fields exists only for the lowest temperature measurements at 2 K (Figure S3b), whereas the measurements match at higher temperatures. This behavior is therefore likely explained by the magnetocaloric effect:[44] in pulsed magnetic fields, the thermal coupling to the bath is too slow to achieve perfect thermalization, and so the decrease in entropy as the spins align on the upsweep drives a rise in lattice entropy, bringing the sample briefly to a temperature at which the level crossing cannot be observed. Conversely, in DC magnetic fields, the sweep rate is much slower and the thermal coupling to the bath fixes the sample at the intended measurement temperature. This effect is more pronounced at lower temperatures, explaining the low temperature behavior in pulsed magnetic field magnetization data.

The magnetocaloric effect may also be responsible for the lack of sharpness of the plateaus observed in the magnetization data at the lowest temperatures, e.g., at 0.5 K in Figure 2c,d. First, note from Figure 4d that while very low temperatures show sharp plateaus, as the temperature increases, this instead forms a positively correlated M (H) curve with fluctuating slope. Therefore, "plateaus" in this case are identified by inflection points rather than regions of zero slope. However, at 0.5 K, we might expect these features to be sharper. Instead we observe that the 1.5 and 0.4 K data in Figure 2c look similar. Since the magnetocaloric effect causes the largest increase in temperature when the initial temperature is lowest, this unexpected similarity is well-explained by the magnetocaloric effect.

We also note that the first magnetization plateau at lowest magnetic fields is dominated by an alignment of the spins to the magnetic field, and contains a small contribution from the level crossing. This would explain the minimal electric polarization change at that first plateau, whereas all other plateaus produce significant changes in electric polarization.

CONCLUSION

Magnetoelectric coupling at spin level crossings in applied magnetic fields is demonstrated in the mixed-valence metal–organic molecule, $[NaMn^{II}Mn_3^{III}(\mu_4\text{-}O)(HL)_3(NCS)_4]$. Magnetization measurements demonstrate a series of plateaus, which are explained well by modeling the ground-state level crossings. This model also predicts the behavior that was subsequently observed in 73 T magnetization measurements. Electric polarization measurements show similar high magnetic field features to the magnetization and at high magnetic field. Conversely, the lowest magnetic field magnetization plateau is dominated not by a spin level crossing but by paramagnetic alignment of the spins. For this reason, the increase in magnetization is not accompanied by a corresponding change in electrical polarization.

The ME coupling behavior observed in **Mn_4Na**, coupled exclusively to spin level crossings driven by Zeeman splitting, is unusual in molecule-based magnetic materials. Moreover, while the magnetic fields at which this behavior is observed are very high, the magnitude of the change in electric polarization is also very high. At 73 T, the change in polarization relative to $H = 0$ T is 100 $\mu C/m^2$, which is approximately 2% of the record for any compound.[45] If we use a linear fit on the approximately linear part of the $P(H)$ data in Figure 3c, we get an expected polarization change at 100 T of ~170 $\mu C/m^2$, which is about 3.5% of the record. These values are on the same order of magnitude as those reported in recent spin crossover studies.[29,30]

Magnetoelectric coupling in molecule-based magnetic materials remains a relatively nascent field. This exploration of coupling between spin level crossings and electric polarization paves the way toward controlling and sensing spin levels with electric fields. More broadly, this study and future measurements aimed at discovering new families of materials with magnetoelectric coupling and expanding existing families are quite promising and may help pave the way to better functional materials for use in technologies built on the magnetoelectric effect.

EXPERIMENTAL SECTION

Single crystals of **Mn_4Na** were grown according to the previously reported procedure.[35] The reaction was carried out under inert atmosphere using standard Schlenk techniques. Commercial starting materials $Mn(ClO_4)_2{\cdot}6H_2O$ (reagent grade, Alfa Aesar), NaOMe (97%, Fluka Analytical), and KSCN (98%, EMD) were used as received. The Schiff-base ligand precursor H_3L was synthesized as per reported procedure.[46]

$[NaMn^{II}Mn_3^{III}(\mu_4\text{-}O)(HL)_3(NCS)_4]$ (Mn_4Na): the ligand precursor H_3L (99 mg, 0.50 mmol) was added slowly to a solution of $Mn(ClO_4)_2{\cdot}H_2O$ (180 mg, 0.490 mmol) in 30 mL of methanol. While the solution was stirred, solid NaOMe (27.6 mg, 0.51 mmol) and KSCN (98.0 mg, 1.01 mmol) were added after 10 and 20 min, respectively. The mixture was stirred at room temperature for 6 h, and the resulting dark-brown solution was filtered through a glass frit. The filtrate was left undisturbed for slow evaporation under inert atmosphere of N_2 gas. The crystals obtained after 2 weeks were harvested, washed successively by ice-cold methanol and diethyl ether, and dried in air. Yield = 54 mg (30%). Details of crystal structure determination and refinement are provided in the Supporting Information file. The final structural parameters have been deposited with the Cambridge Crystallographic Data Centre (CCDC) under deposition number 2376419.

Magnetization measurements were taken in both DC and pulsed magnetic fields. In order to prepare for both types of measurements, samples were inserted into a custom capsule necessary for pulsed magnetic field measurements. These

https://doi.org/10.1021/jacs.4c07759
J. Am. Chem. Soc. 2024, 146, 32383−32391

capsules are ∼1 mm in diameter and ∼2 mm in length and made of PCTFE.

DC measurements were taken using a 14 T quantum design physical property measurement system (PPMS) using their vibrating sample magnetometry (VSM) module. Since it was necessary to use DC measurements to calibrate the pulsed magnetic field measurements (see Supporting Information), the sample used in pulsed magnetic field measurements in its capsule was inserted into a second capsule meant for VSM measurements. By measuring each temperature twice—once with the sample and pulsed magnetic field capsule and once without—it was possible to get a background subtracted measurement that was exactly comparable to the pulsed magnetic field measurements.

Pulsed magnetic field measurements[47] were collected in capacitor-driven magnets using 1.5 mm inner-diameter copper coils to record the change in magnetization. The coil is compensated—the inner windings are clockwise and the outer windings are clockwise, to remove the contribution of a radially uniform magnetic field. Thus, the contribution from the sample only is recorded, whose magnetic field varies between the inner and outer diameter of the coil. The coil is additionally dynamically compensated with a few coil loops, whose contribution is electronically added or subtracted, to correct for thermal contraction. Finally, the data is collected for the sample and its capsule in and out of the coil, by in situ removing the sample using a rod without changing the temperature, and measuring nearly identical magnetic field pulses.

Electric polarization measurements were taken using custom probes with GORE coaxial cables in both the DC and pulsed magnetic field measurements.[18,29] In DC magnetic fields the magnetoelectric current (change in electric polarization with time) was recorded by an Keithley 6517 electrometer, and in pulsed magnetic fields by a Stanford Research 570 current-to-voltage converter. The raw dP/dt data was integrated in time to obtain ΔP with respect to zero magnetic field. To determine the value of ΔP in C/m^2, the sample was modeled as a parallel plate capacitor and ImageJ was used to obtain the area of the silver paint lead, approximating the sample as a parallel plate capacitor (see Supporting Information).[48]

■ ASSOCIATED CONTENT

Supporting Information

The Supporting Information is available free of charge at https://pubs.acs.org/doi/10.1021/jacs.4c07759.

> Additional magnetization measurements demonstrating reproducibility and information on calibration of magnetization measurements performed in pulsed magnetic fields; complementary polarization data taken with $H||E||c$ axis and explanation of image analysis of electrical leads; additional complementary theory calculations (PDF)

Accession Codes

Deposition Number 2376419 contains the supplementary crystallographic data for this paper. These data can be obtained free of charge via the joint Cambridge Crystallographic Data Centre (CCDC) and Fachinformationszentrum Karlsruhe Access Structures service.

■ AUTHOR INFORMATION

Corresponding Authors

James Paris Wampler − *National High Magnetic Field Lab, Los Alamos National Lab, Los Alamos, New Mexico 87545, United States;* orcid.org/0000-0003-4776-1897; Email: jamespwampler@gmail.com

Michael Shatruk − *Department of Chemistry and Biochemistry, Florida State University, Tallahassee, Florida 32306, United States*; Email: shatruk@chem.fsu.edu

Vivien S. Zapf − *National High Magnetic Field Lab, Los Alamos National Lab, Los Alamos, New Mexico 87545, United States;* orcid.org/0000-0002-8375-4515; Email: vzapf@lanl.gov

Authors

Shuanglong Liu − *Department of Physics, Northeastern University, Boston, Massachusetts 02115, United States; Center for Molecular Magnetic Quantum Materials, University of Florida, Gainesville, Florida 32611, United States*

Dibya Jyoti Mondal − *Department of Chemistry and Biochemistry, Florida State University, Tallahassee, Florida 32306, United States;* orcid.org/0000-0002-6778-9339

Magdalena Owczarek − *National High Magnetic Field Lab, Los Alamos National Lab, Los Alamos, New Mexico 87545, United States*

Shengzhi Zhang − *National High Magnetic Field Lab, Los Alamos National Lab, Los Alamos, New Mexico 87545, United States*

Ping Wang − *Department of Chemistry and Biochemistry, Florida State University, Tallahassee, Florida 32306, United States*

Miguel Gakiya-Teruya − *Department of Chemistry and Biochemistry, Florida State University, Tallahassee, Florida 32306, United States*

Minseong Lee − *National High Magnetic Field Lab, Los Alamos National Lab, Los Alamos, New Mexico 87545, United States*

Hai-Ping Cheng − *Department of Physics, Northeastern University, Boston, Massachusetts 02115, United States; Center for Molecular Magnetic Quantum Materials, University of Florida, Gainesville, Florida 32611, United States;* orcid.org/0000-0001-5990-1725

Complete contact information is available at: https://pubs.acs.org/10.1021/jacs.4c07759

Notes

The authors declare no competing financial interest.

■ ACKNOWLEDGMENTS

The scientific work was primarily funded by the Center for Molecular Magnetic Quantum Materials (M2QM), an Energy Frontier Research Center (EFRC) funded by the U.S. Department of Energy (DOE), Office of Science, Basic Energy Sciences under Award DE-SC0019330. An initial portion of M.O. and J.W.'s time was funded by the LANL LDRD program. The high-field facility was provided by the National High Magnetic Field Laboratory, supported by National Science Foundation and the U.S. Department of Energy Cooperative Agreement Nos. DMR-1644779 and DMR-2128556* and the State of Florida. The calculations employed resources of the University of Florida Research Computing as

well as the National Energy Research Scientific Computing Center (NERSC), a U.S. Department of Energy Office of Science User Facility located at Lawrence Berkeley National Laboratory, operated under Contract No. DE-AC02-05CH11231 using NERSC award BES-ERCAP0022828. This project also used resources provided by the X-ray Crystallography Center (FSU075000XRAY) at the Department of Chemistry and Biochemistry, Florida State University.

REFERENCES

(1) Hornreich, R. M. The Magnetoelectric Effect: Materials, Physical Aspects, and Applications. *IEEE Trans. Magn.* **1972**, *8*, 584−589.
(2) Fiebig, M. Revival of the Magnetoelectric Effect. *J. Phys. D: Appl. Phys.* **2005**, *38*, R123−R152.
(3) Spaldin, N. A.; Ramesh, R. Advances in magnetoelectric multiferroics. *Nat. Mater.* **2019**, *18*, 203−212.
(4) Liang, X.; Chen, H.; Sun, N. X. Magnetoelectric materials and devices. *APL Mater.* **2021**, *9* (4), 041114.
(5) Kopyl, S.; Surmenev, R.; Surmeneva, M.; Fetisov, Y.; Kholkin, A. Magnetoelectric effect: principles and applications in biology and medicine- a review. *Mater. Today Bio.* **2021**, *12*, 100149.
(6) Astrov, D. N. The Magnetoelectric Effect in Antiferromagnetics. *Sov. Phys. JETP* **1960**, *11*, 708−709.
(7) Rado, G. T.; Folen, V. J. Observation of the Magnetically Induced Magnetoelectric Effect and Evidence for Antiferromagnetic Domains. *Phys. Rev. Lett.* **1961**, *7* (8), 310−311.
(8) Pradhan, D. K.; Kumari, S.; Rack, P. D. Magnetoelectric Composites: Applications, Coupling Mechanisms, and Future Directions. *Nanomaterials* **2020**, *10* (10), 2072.
(9) Bichurin, M.; Petrov, R.; Sokolov, O.; Leontiev, V.; Kuts, V.; Kiselev, D.; Wang, Y. Magnetoelectric magnetic field sensors: A review. *Sensors* **2021**, *21*, 6232.
(10) Kosub, T.; Kopte, M.; Hühne, R.; Appel, P.; Shields, B.; Maletinsky, P.; Hübner, R.; Liedke, M. O.; Fassbender, J.; Schmidt, O. G.; Makarov, D. Purely antiferromagnetic magnetoelectric random access memory. *Nat. Commun.* **2017**, *8* (1), 13985.
(11) Amiri, P. K.; Alzate, J. G.; Cai, X. Q.; Ebrahimi, F.; Hu, Q.; Wong, K.; Grezes, C.; Lee, H.; Yu, G.; Li, X.; Akyol, M.; et al. Electric-Field-Controlled Magnetoelectric RAM: Progress, Challenges, and Scaling. *IEEE Trans. Magn.* **2015**, *51* (11), 1−7.
(12) Hill, S.; Edwards, R. S.; Aliaga-Alcalde, N.; Christou, G. Quantum Coherence in an Exchange-Coupled Dimer of Single-Molecule Magnets. *Science* **2003**, *302*, 1015−1018.
(13) Gaita-Ariño, A.; Luis, F.; Hill, S.; Coronado, E. Molecular spins for quantum computation. *Nat. Chem.* **2019**, *11*, 301−309.
(14) Coronado, E. Molecular magnetism: from chemical design to spin control in molecules, materials and devices. *Nat. Rev. Mater.* **2020**, *5*, 87−104.
(15) Trif, M.; Troiani, F.; Stepanenko, D.; Loss, D. Spin-electric coupling in molecular magnets. *Phys. Rev. Lett.* **2008**, *101*, 217201.
(16) Bulaevskii, L. N.; Batista, C. D.; Mostovoy, M. V.; Khomskii, D. I. Electronic orbital currents and polarization in Mott insulators. *Phys. Rev. B* **2008**, *78*, 024402.
(17) Liu, Z.; Wang, Y. X.; Fang, Y. H.; Qin, S. X.; Wang, Z. M.; Jiang, S. D.; Gao, S. Electric field manipulation enhanced by strong spin-orbit coupling: Promoting rare-earth ions as qubits. *Natl. Sci. Rev.* **2020**, *7*, 1557−1563.
(18) Zapf, V. S.; Kenzelmann, M.; Wolff-Fabris, F.; Balakirev, F.; Chen, Y. Magnetically induced electric polarization in an organometallic magnet. *Phys. Rev. B* **2010**, *82* (6), 060402.
(19) Zapf, V. S.; Sengupta, P.; Batista, C. D.; Nasreen, F.; Wolff-Fabris, F.; Paduan-Filho, A. Magnetoelectric effects in an organometallic quantum magnet. *Phys. Rev. B* **2011**, *83* (14), 140405.
(20) Boudalis, A. K.; Robert, J.; Turek, P. First Demonstration of Magnetoelectric Coupling in a Polynuclear Molecular Nanomagnet: Single-Crystal EPR Studies of $[Fe_3O(O_2CPh)_6(py)_3]ClO_4$·py under Static Electric Fields. *Chem.—Eur. J.* **2018**, *24*, 14896−14900.
(21) Liu, J.; Mrozek, J.; Myers, W. K.; Timco, G. A.; Winpenny, R. E.; Kintzel, B.; Plass, W.; Ardavan, A. Electric Field Control of Spins in Molecular Magnets. *Phys. Rev. Lett.* **2019**, *122*, 037202.
(22) Kintzel, B.; Fittipaldi, M.; Böhme, M.; Cini, A.; Tesi, L.; Buchholz, A.; Sessoli, R.; Plass, W. Spin-Electric Coupling in a Cobalt(II)-Based Spin Triangle Revealed by Electric-Field-Modulated Electron Spin Resonance Spectroscopy. *Angew. Chem., Int. Ed.* **2021**, *60*, 8832−8838.
(23) Lewkowitz, M.; Adams, J.; Sullivan, N. S.; Wang, P.; Shatruk, M.; Zapf, V.; Arvij, A. S. Direct observation of electric field-induced magnetism in a molecular magnet. *Sci. Rep.* **2023**, *13* (1), 2769.
(24) Wang, Y.-X.; Su, D.; Ma, Y.; Sun, Y.; Cheng, P. Electrical detection and modulation of magnetism in a Dy-based ferroelectric single-molecule magnet. *Nat. Commun.* **2023**, *14* (1), 7901.
(25) Jain, P.; Ramachandran, V.; Clark, R. J.; Zhou, H. D.; Toby, B. H.; Dalal, N. S.; Kroto, H. W.; Cheetham, A. K. Multiferroic Behavior Associated with an Order−Disorder Hydrogen Bonding Transition in Metal−Organic Frameworks (MOFs) with the Perovskite ABX_3 Architecture. *J. Am. Chem. Soc.* **2009**, *131*, 13625−13627.
(26) Ramesh, R. Emerging routes to multiferroics. *Nature* **2009**, *461*, 1218−1219.
(27) Wang, W.; Yan, L. Q.; Cong, J. Z.; Zhao, Y. L.; Wang, F.; Shen, S. P.; Zou, T.; Zhang, D.; Wang, S. G.; Han, X. F.; Sun, Y. Magnetoelectric coupling in the paramagnetic state of a metal-organic framework. *Sci. Rep.* **2013**, *3* (1), 2024.
(28) Gómez-Aguirre, L. C.; Pato-Doldán, B.; Mira, J.; Castro-García, S.; Senñarís-Rodríguez, M. A.; Sánchez-Andújar, M.; Singleton, J.; Zapf, V. S. Magnetic Ordering-Induced Multiferroic Behavior in $[CH_3NH_3][Co(HCOO)_3]$ Metal-Organic Framework. *J. Am. Chem. Soc.* **2016**, *138*, 1122−1125.
(29) Chikara, S.; Gu, J.; Zhang, X. G.; Cheng, H. P.; Smythe, N.; Singleton, J.; Scott, B.; Krenkel, E.; Eckert, J.; Zapf, V. S. Magnetoelectric behavior via a spin state transition. *Nat. Commun.* **2019**, *10* (1), 4043.
(30) Jakobsen, V. B.; Chikara, S.; Yu, J. X.; Dobbelaar, E.; Kelly, C. T.; Ding, X.; Weickert, F.; Trzop, E.; Collet, E.; Cheng, H. P.; Morgan, G. G.; Zapf, V. S. Giant Magnetoelectric Coupling and Magnetic-Field-Induced Permanent Switching in a Spin Crossover Mn(III) Complex. *Inorg. Chem.* **2021**, *60*, 6167−6175.
(31) Owczarek, M.; Lee, M.; Liu, S.; Blake, E. R.; Taylor, C. S.; Newman, G. A.; Eckert, J. C.; Leal, J. H.; Semelsberger, T. A.; Cheng, H. P.; Nie, W.; Zapf, V. S. Near-Room-Temperature Magnetoelectric Coupling via Spin Crossover in an Iron(II) Complex. *Angew. Chem., Int. Ed.* **2022**, *61* (52), No. e202214335.
(32) Zhang, X.; Xu, W. H.; Zheng, W.; Su, S. Q.; Huang, Y. B.; Shui, Q.; Ji, T.; Uematsu, M.; Chen, Q.; Tokunaga, M.; Gao, K.; Okazawa, A.; Kanegawa, S.; Wu, S. Q.; Sato, O. Magnetoelectricity Enhanced by Electron Redistribution in a Spin Crossover [FeCo] Complex. *J. Am. Chem. Soc.* **2023**, *145*, 15647−15651.
(33) Islam, M. F.; Nossa, J. F.; Canali, C. M.; Pederson, M. First-principles study of spin-electric coupling in a Cu_3 single molecular magnet. *Phys. Rev. B* **2010**, *82*, 155446.
(34) Spaldin, N. A.; Fiebig, M.; Mostovoy, M. The toroidal moment in condensed-matter physics and its relation to the magnetoelectric effect. *J. Phys.: Condens. Matter* **2008**, *20*, 434203.
(35) Yang, P. P.; Zhu, L. L.; Xu, Y.; Shao, C. Y. Synthesis, crystal structures, and magnetic properties of two tetrahedral $Mn^{II}Mn^{III}_3$ complexes. *Zeitschrift Fur Anorganische Und Allgemeine Chem.* **2013**, *639*, 1821−1826.
(36) Manoli, M.; Johnstone, R. D.; Parsons, S.; Murrie, M.; Affronte, M.; Evangelisti, M.; Brechin, E. K. A Ferromagnetic Mixed-Valent Mn Supertetrahedron: Towards Low-Temperature Magnetic Refrigeration with Molecular Clusters. *Angew. Chem., Int. Ed.* **2007**, *46*, 4456−4460.
(37) Miyasaka, H.; Nakata, K.; Sugiura, K. I.; Yamashita, M.; Clérac, R. A Three-Dimensional Ferrimagnet Composed of Mixed-Valence Mn_4 Clusters Linked by an $Mn[N(CN)_2]_6^{4-}$ Unit. *Angew. Chem., Int. Ed.* **2004**, *43*, 707−711.

(38) Yoo, J.; Yamaguchi, A.; Nakano, M.; Krzystek, J.; Streib, W. E.; Brunel, L. C.; Ishimoto, H.; Christou, G.; Hendrickson, D. N. Mixed-Valence Tetranuclear Manganese Single-Molecule Magnets. *Inorg. Chem.* **2001**, *40*, 4604−4616.
(39) Sessoli, R.; Tsai, H.-L.; Schake, A. R.; Wang, S.; Vincent, J. B.; Folting, K.; Gatteschi, D.; Christou, G.; Hendrickson, D. N. High-Spin Molecules: $[Mn_{12}O_{12}(O_2CR)_{16}(H_2O)_4]$. *J. Am. Chem. Soc.* **1993**, *115*, 1804−1816.
(40) Sessoli, R.; Gatteschi, D.; Caneschi, A.; Novakt, M. A. Magnetic bistability in a metal-ion cluster. *Nature* **1993**, *365*, 141−143.
(41) Soler, M.; Wernsdorfer, W.; Folting, K.; Pink, M.; Christou, G. Single-Molecule Magnets: A Large Mn_{30} Molecular Nanomagnet Exhibiting Quantum Tunneling of Magnetization. *J. Am. Chem. Soc.* **2004**, *126*, 2156−2165.
(42) Murugesu, M.; Habrych, M.; Wernsdorfer, W.; Abboud, K. A.; Christou, G. Single-Molecule Magnets: A Mn_{25} Complex with a Record S=51/2 Spin for a Molecular Species. *J. Am. Chem. Soc.* **2004**, *126*, 4766−4767.
(43) Tasiopoulos, A. J.; Vinslava, A.; Wernsdorfer, W.; Abboud, K. A.; Christou, G. Giant single-molecule magnets: A Mn_{84} torus and its supramolecular nanotubes. *Angew. Chem., Int. Ed.* **2004**, *43*, 2117−2121.
(44) Kohama, Y.; Marcenat, C.; Klein, T.; Jaime, M. AC measurement of heat capacity and magnetocaloric effect for pulsed magnetic fields. *Rev. Sci. Instrum.* **2010**, *81* (10), 104902.
(45) Aoyama, T.; Yamauchi, K.; Iyama, A.; Picozzi, S.; Shimizu, K.; Kimura, T. Giant spin-driven ferroelectric polarization in $TbMnO_3$ under high pressure. *Nat. Commun.* **2014**, *5*, 4927.
(46) Boskovic, C.; Rusanov, E.; Stoeckli-Evans, H.; Gudel, H. U. New tri- and tetranuclear transition metal spin clusters incorporating a versatile polydentate Schiff base ligand. *Inorg. Chem. Commun.* **2002**, *5*, 881−886.
(47) Detwiler, J. A.; Schmiedeshoff, G. M.; Harrison, N.; Lacerda, A. H.; Cooley, J. C.; Smith, J. L. Magnetization of UBe_{13} to 60 T. *Phys. Rev. B* **2000**, *61*, 402−404.
(48) Schneider, C. A.; Rasband, W. S.; Eliceiri, K. W. NIH Image to ImageJ: 25 years of image analysis. *Nat. Methods* **2012**, *9*, 671−675.

https://doi.org/10.1021/jacs.4c07759
J. Am. Chem. Soc. 2024, 146, 32383−32391